Uncertainty quantification in a macroscopic traffic flow model calibrated on GPS data

Enrico Bertino[1] Régis Duvigneau[2] Paola Goatin[2]

Abstract

The objective of this paper is to analyze the inclusion of one or more random parameters into the deterministic Lighthill-Whitham-Richards traffic flow model and use a semi-intrusive approach to quantify uncertainty propagation. To verify the validity of the method, we test it against real data coming from vehicle embedded GPS systems, provided by Autoroutes Trafic.

Keywords: Macroscopic traffic flow models; stochastic conservation laws; uncertainty quantification; stochastic parameters; real data.

1 Introduction

Macroscopic traffic flow models consisting in (systems of) partial differential equations are used to simulate traffic flows on road networks since decades [25]. Yet, these models are usually fully deterministic, and the coupling with real data poses severe difficulties, which require advanced data assimilation techniques (see e.g. [29] and references therein) and may result in poor prediction outcomes.

In this paper, we focus on the basic Lightwill-Whitham-Richards (LWR) first order model [17, 22], augmented with random variables in the velocity function and the initial condition to account for real data uncertainty. This model is specifically designed to cope with the traffic data set we were provided, which consists of floating car data coming from embedded GPS devices. For alternative stochastic traffic flow models, we refer the reader to [4, 7, 14, 16, 23, 24, 27].

Several stochastic methods have been proposed in literature to evaluate uncertainty propagation in stochastic PDE models. The so-called *non-intrusive* methods, like Monte Carlo or stochastic collocation [18], allow to use the underlying deterministic code but suffer of slow convergence rate and curse of dimensionality. On the other side, *intrusive* methods, like polynomial chaos expansion [21], require deep modifications of the deterministic simulation code and are not suitable for discontinuous solutions. In this work, we choose the *semi-intrusive* approach proposed by Abgrall and Congedo [3]. The underlying idea is to extend the spatial computational domain to the probabilistic components and to compute conditional expectations of the flux in the probabilistic direction. To evaluate the expectations of the flux, we use a piecewise polynomial approximation computed using a reconstruction method. This polynomial reconstruction is the same used for space finite volume methods, except that the

[1]Politecnico di Milano, Piazza Leonardo da Vinci 32, 20133 Milan, Italy. E-mail: enrico.bertino91@gmail.com

[2]Inria Sophia Antipolis - Méditerranée, Université Côte d'Azur, Inria, CNRS, LJAD, 2004 route des Lucioles - BP 93, 06902 Sophia Antipolis Cedex, France. E-mail: {regis.duvigneau, paola.goatin}@inria.fr

measure is no longer the standard Lebesgue measure but the probabilistic one. Compared to the above mentioned approaches, the Abgrall-Congedo method requires minor modification of the deterministic code and ensure rapid convergence. It can be applied to any probability distribution function, in case of correlated random variables and it is suitable to discontinuous solutions.

We test the model against real data collected in the sector between Antibes and Nice of the French highway A8, la Provençale. This section is very busy and is suitable to study congested traffic. For this analysis, we rely on preliminary data treatment and model calibration preformed in [6].

The paper is organized as follows. Section 2 describes the data set. In Section 3 we recall the deterministic LWR model and the corresponding numerical scheme used later. In Section 4 we introduce the stochastic setting and the random variables of interest. The semi-intrusive approach is described and tested in Section 5. Section 6 is devoted to validation against real data and conclusion and perspectives are presented in Section 7.

2 GPS data: a case study

The traffic data available for this research were provided by the company AUTOROUTES TRAFIC [1] and they are presented and treated in [6, Section 4]. They correspond to a sector of the French A8 highway, also called *la Provençale*, between the exit no. 45 (Antibes) and the exit no. 49 (Nice St Isidore), for a total length of 17,5 km, see Figure 1a. In this study, we will consider the direction from Antibes to Nice St Isidore, denoted as *Direction 1*.
Data were collected on four Tuesdays (March 19 and 26 and April 2 and 9, 2013) from 6 a.m. to 11 a.m. and are divided into two categories: GPS data and magnetic loop detector data. GPS data, supplied by COYOTE embedded systems, include the device ID, the position and the velocity of the car, sent every minute. In order to show the behaviour of data, in Figure 1b we report in a space-time plot the speeds registered on March 19. Loop detector data are

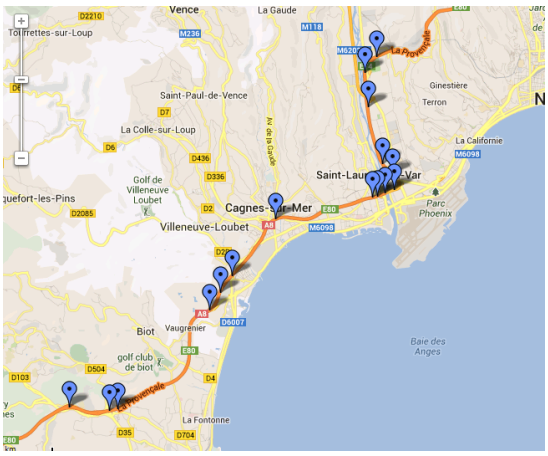

(a) The considered section of A8 highway, with the location of the loop detectors (map data: @2013 Google).

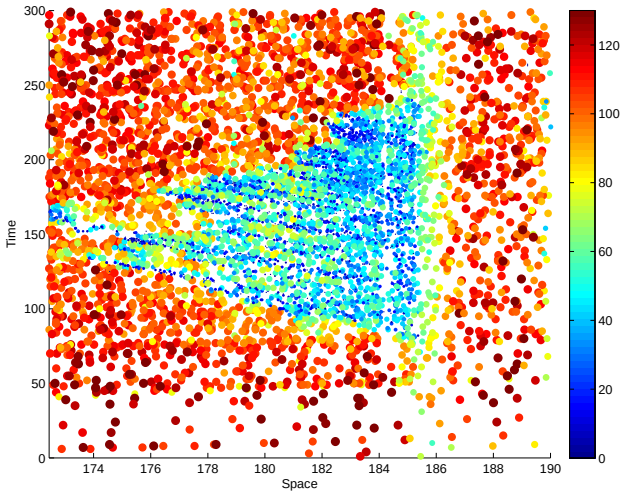

(b) Scatterplot of GPS data of March 19$^{\text{th}}$, taken from [6].

Figure 1: The A8 highway between Antibes and Nice.

supplied by the highway operator ESCOTA [2] at 16 locations and consist of hourly and 6 min flux averages. They will be used for the estimation of the real amount of cars travelling on the considered section, see Section 4.2.

3 The deterministic LWR model

Macroscopic traffic flow models describe the evolution of the position of vehicles on a (infinite) road identified with the real line in terms of averaged quantities, such as the density $\rho = \rho(t, x)$, $t \in \mathbb{R}_+, x \in \mathbb{R}$ and the average speed of cars $v = v(t, x)$. The first model was introduces in the mid '50 by Lighthill, Whitham and Richards [17, 22] and it is based on the conservation of the number of cars, which is expressed by the following scalar conservation law:

$$\frac{\partial}{\partial t}\,\rho(x,t) + \frac{\partial}{\partial x}\,q(x,t) = 0, \tag{3.1}$$

where $q = \rho v$ is the traffic flow. To close the equation, the LWR model assumes that $v = v(\rho)$ is a non-increasing function of the density. In this work, we will use a modified Newell-Daganzo velocity function [9, 20], which is characterized by a linear decreasing free-flow speed and a hyperbolic velocity in congested regime, and we add a downward jump at $\rho = \rho_c$ to model the capacity drop observed in real traffic (cf. Fig. 2):

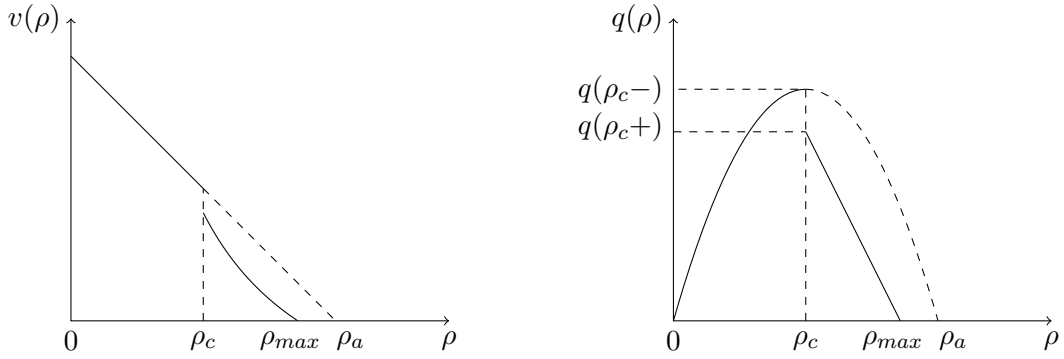

(a) Velocity function **(b)** Flux function

Figure 2: Fundamental diagram with capacity drop.

$$v(\rho) = \begin{cases} v_{max}\left(1 - \dfrac{\rho}{\rho_a}\right) & \text{if } 0 \le \rho \le \rho_c, \\ -\omega_f\left(1 - \dfrac{\rho_{max}}{\rho}\right) & \text{if } \rho_c < \rho \le \rho_{max}, \end{cases} \tag{3.2}$$

where v_{max} is the maximal free-flow speed, ω_f is the backward propagating wave-speed, ρ_c is the critical density (the limit density between the fluid and congested phases), ρ_{max} is the maximal density corresponding to a bumper-to-bumper situation and ρ_a is a further parameter accounting for the capacity drop, so that

$$v_{max}\left(1 - \frac{\rho_c}{\rho_a}\right) > -\omega_f\left(1 - \frac{\rho_{max}}{\rho_c}\right). \tag{3.3}$$

This choice has shown to best fit our data, as results from [6].

Approximate solutions to (3.1) can be computed via Godunov finite volume method [13], which is equivalent to the supply-demand method (or Cell Transmission Model) used by the transportation engineers [9, 11, 15].

Let Δx and Δt be respectively the space and time grid sizes, $x_i = i\Delta x$, $i \in \mathbb{Z}$, be the grid points and $C_i = [x_{i-1/2}, x_{i+1/2}[$ the space mesh cells. We aim at constructing approximate solutions

$$\rho_\Delta(t,x) := \rho_i^n \quad \text{for } (t,x) \in [t^n, t^{n+1}[\times[x_{i-1/2}, x_{i+1/2}[, \qquad i \in \mathbb{Z}, n \in \mathbb{N}.$$

In order to iteratively define ρ_Δ, the demand and supply functions are usually defined respectively as

$$D(\rho) = \begin{cases} q(\rho) & \text{if } 0 \le \rho \le \rho_c, \\ q(\rho_c) & \text{if } \rho_c < \rho \le \rho_{max}, \end{cases} \qquad S(\rho) = \begin{cases} q(\rho_c) & \text{if } 0 \le \rho \le \rho_c, \\ q(\rho) & \text{if } \rho_c < \rho \le \rho_{max}. \end{cases}$$

In the case of a discontinuous flux function, the above definitions are modified as follow [28]:

$$\begin{array}{ll} \text{if } \rho_i < \rho_c & D(\rho_i) = \min\{q(\rho_i), q(\rho_c+)\}, \\ \text{if } \rho_i > \rho_c & D(\rho_i) = q(\rho_c-), \\ \text{if } \rho_i = \rho_c & \text{if } \rho_{i+1} < \rho_c,\ D(\rho_i) = q(\rho_c-), \\ & \text{if } \rho_{i+1} > \rho_c,\ D(\rho_i) = q(\rho_c+), \\ \text{if } \rho_{i+1} < \rho_c & S(\rho_{i+1}) = q(\rho_c-), \\ \text{if } \rho_{i+1} > \rho_c & S(\rho_{i+1}) = q(\rho_{i+1}), \\ \text{if } \rho_{i+1} = \rho_c & \ell = \min\{l : l > i+1 < l \text{ and } \rho_l \neq \rho_c\}, \\ & \text{if } \rho_\ell < \rho_c,\ S(\rho_{i+1}) = q(\rho_c-), \\ & \text{if } \rho_\ell > \rho_c,\ S(\rho_{i+1}) = q(\rho_c+), \\ & \text{if } \nexists \ell,\ S(\rho_{i+1}) = q(\rho_c-), \\ \text{if } \rho_i = \rho_{i+1} = \rho_c & D(\rho_i) = S(\rho_{i+1}), \end{array} \tag{3.4}$$

where $q(\rho_c\pm)$ denote the left and right traces of q at ρ_c.

The Godunov numerical flux at the interface $x_{i+1/2}$ is then defined by

$$h^G(\rho_i, \rho_{i+1}) = \min\{D(\rho_i), S(\rho_{i+1})\}, \tag{3.5}$$

and the recursive numerical scheme is given by

$$\rho_i^{n+1} = \rho_i^n - \frac{\Delta t}{\Delta x}\left(h^G(\rho_i^n, \rho_{i+1}^n) - h^G(\rho_{i-1}^n, \rho_i^n)\right), \qquad i \in \mathbb{Z}, n \in \mathbb{N}, \tag{3.6}$$

under the classical CFL condition

$$\Delta t\ \lambda^n \le \Delta x,$$

where λ^n is the maximum of the absolute values of wave speeds at time t^n, see [28, Section 5] for more details. The scheme (3.6) is initialized taking

$$\rho_i^0 = \frac{1}{\Delta x}\int_{x_{i-1/2}}^{x_{i+1/2}} \rho_0(x)\ dx, \qquad i \in \mathbb{Z},$$

for a given initial datum $\rho_0 : \mathbb{R} \to [0, \rho_{max}]$.

4 Stochastic scalar conservation laws

Following [18, 19, 26], we will consider $N = 2$ independent random variables $X := \{X_1, X_2\}$ defined on a probability space $\mathcal{P} = (\Omega, \mathcal{B}_\Omega, \mu)$, where $\omega := (\omega_1, \dots, \omega_s) \in \Omega := \Pi_{i=1}^s [a_i, b_i]$ is the sample space of random parameters, $\mathcal{B}_\Omega$ is the σ-algebra of the Borel sets on Ω and μ the Lebesgue measure. We assume that $X_i : \Omega \to \mathbb{R}$ is measurable and we denote by $f_{X_i} : \mathbb{R} \to \mathbb{R}_+$ its probability density function. Since the variable are independent, their cumulative distribution is given by $f_X(x_1, x_2) = f_{X_1}(x_1) f_{X_2}(x_2)$. Hence, for any measurable real valued function g, its expected value is given by

$$E[g(X)] = \int_\Omega g(X(\omega)) f_X(X(\omega))\, dX(\omega) = \int_{-\infty}^{+\infty} \int_{-\infty}^{+\infty} g(x_1, x_2) f_X(x_1, x_2)\, dx_1\, dx_2.$$

We are interested in the stochastic Cauchy problem

$$\begin{cases} \dfrac{\partial}{\partial t}\ \rho(t, x, \omega) + \dfrac{\partial}{\partial x}\ F(\rho(t, x, \omega); X_1(\omega)) = 0, \quad t > t_0, x \in \mathbb{R}, \omega \in \Omega, \\ \rho(t_0, x, \omega) = \rho_0(x; X_2(\omega)), \end{cases} \tag{4.1}$$

where $F = F(\cdot; X_1(\cdot)) : (\Omega, \mathcal{B}_\Omega) \to (L^\infty(\mathbb{R}; \mathbb{R}); \mathcal{B}(L^\infty(\mathbb{R}; \mathbb{R})))$ is the stochastic flux function and $\rho_0 = \rho_0(\cdot; X_2(\cdot)) : (\Omega, \mathcal{B}_\Omega) \to \left(L^1(\mathbb{R}; \mathbb{R}); \mathcal{B}(L^1(\mathbb{R}, \mathbb{R}))\right)$ the stochastic initial condition. Since we are led to consider flux functions with jump discontinuity in ρ, we refer to the corresponding theory [5, 10, 12]. Let us assume that $F(\rho; X) := F_-(\rho; X) + (F_+(\rho; X) - F_-(\rho; X))H(\rho - \rho_c)$, where H denotes the Heaviside function and $\tilde{H}$ denotes the multivalued extension of H ($\tilde{H}(0) \in [0, 1]$). We say that F is *jump continuous* at ρ_c if the left and right limits at $\rho = \rho_c$ exist and are finite.

Definition 4.1. (Adapted from [19, Definition 3.2]) A measurable mapping $\rho : (\Omega, \mathcal{B}_\Omega) \to C\left(\mathbb{R}_{t>t_0}; L^1(\mathbb{R}; \mathbb{R})\right)$ is a *random entropy solution* of (4.1) if

- For μ-a.e. $\omega \in \Omega$, it satisfies

$$\int_{t_0}^{+\infty} \int_{-\infty}^{+\infty} \left(\rho(t, x, \omega) \frac{\partial}{\partial t} \phi(t, x) + F(\rho(t, x, \omega); X_1(\omega)) \frac{\partial}{\partial x} \phi(t, x) \right) dx\, dt + \int_{-\infty}^{+\infty} \rho_0(x; X_2(\omega))\, \phi(t_0, x)\, dx = 0$$

  for all test functions $\phi \in C_c^1([t_0, +\infty[\times \mathbb{R}; \mathbb{R})$.

- For μ-a.e. $\omega \in \Omega$ and for each convex entropy $\eta \in C^1(\mathbb{R}; \mathbb{R})$, there exists a function $w \in L^\infty(\mathbb{R}^+ \times \mathbb{R}; [0, 1])$ such that $w(t, x) \in \tilde{H}(\rho(t, x, \omega))$ a. e., it holds

$$\int_{t_0}^{+\infty} \int_{-\infty}^{+\infty} \left(\eta(\rho(t, x, \omega)) \frac{\partial}{\partial t} \phi(t, x) + Q(\rho(t, x, \omega); X_1(\omega)) \frac{\partial}{\partial x} \phi(t, x) + \eta'(\rho_c) \frac{\partial}{\partial x} w(t, x) \right) dx\, dt + \int_{-\infty}^{+\infty} \eta(\rho_0(x; X_2(\omega))) \phi(t_0, x)\, dx \geq 0$$

  for all test functions $\phi \in C_c^1([t_0, +\infty[\times \mathbb{R}; \mathbb{R}_+)$, where

$$Q(\rho; X) = \int_0^\rho \eta'(\sigma) \left[F'_-(\sigma; X) + (F'_+(\sigma; X) - F'_-(\sigma; X)) H(\sigma - \rho_c) \right] d\sigma.$$

Well-posedness results for problem (4.1) in the case $F \in W^{1,\infty}(\mathbb{R}; \mathbb{R})$ can be found in [19, Theorem 3.3] and [18, Theorem 3.11].

4.1 Random velocity

To account for vehicle speed variability, we consider a stochastic velocity function in the form

$$V(\rho; X_1(\omega)) = (1 + X_1(\omega))v(\rho), \qquad X_1 \in [-1, 1], \tag{4.2}$$

expressing the perturbation from the equilibrium velocity v. The distribution of the perturbation depends on several factors as, for instance, the drivers behavior and the weather conditions. We use GPS real data to fit the distribution function. To this end, we plot speed values against densities and we find a spline curve interpolating the medians, separating the density domain in cells and computing the median speed of each spatial cell, see Figure 3. We then compute the y-distance of each point from the spline and, in order to analyze the normality of the distributions, we perform the QQ-plots (Figure 4) in congested and free flow phases separately. Our goal is to apply a suitable perturbation to the velocity in order to reproduce this deviation from a median value. Hence, we have to adjust the parameters of the distribution of these perturbations. We compute the relative distances from the median and we can see their distributions in Figure 5. Their standard deviations are respectively 0.12 and 0.23. For simplification purposes, we will use the same perturbation for free-flow and congested conditions. We take $\sigma = 0.2$, which corresponds to the normal distribution law $N_{(\mu=0,\sigma=0.2)}$. Since we need a distribution with bounded domain, we replace the normal distribution by a triangular law $T_{[-0.5,0,0.5]}$, which still has standard deviation equal to 0.2.

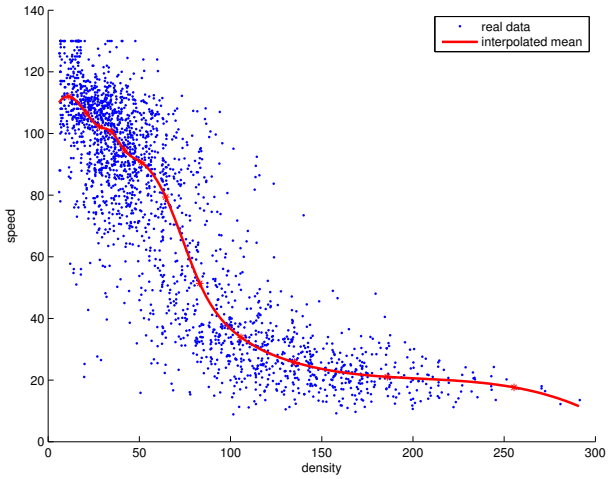

Figure 3: Speed-density fundamental diagram and fitted mean (least squares).

4.2 Random initial datum

The second random variable we consider is a perturbation applied to the initial condition to compensate for the lack of information on the penetration rate of GPS data. In our specific case, the amount of equipped vehicles represents only a little percentage of the total volume of traffic. Its variation depends on the time of the day and, indirectly, on traffic density.
To estimate the percentage of equipped vehicles compared to the total traffic density, we use the corresponding real flux measurements obtained by some magnetic loop detectors. In

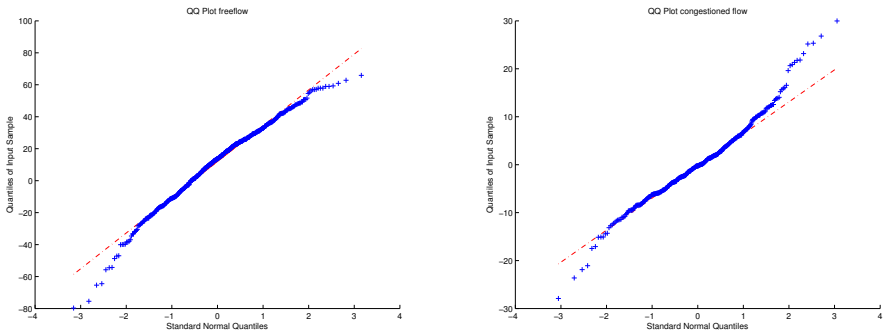

(a) Free flow phase (speed values higher than $70km/h$).

(b) Congested phase (speed values smaller than $70km/h$).

Figure 4: QQ-plots of speed values.

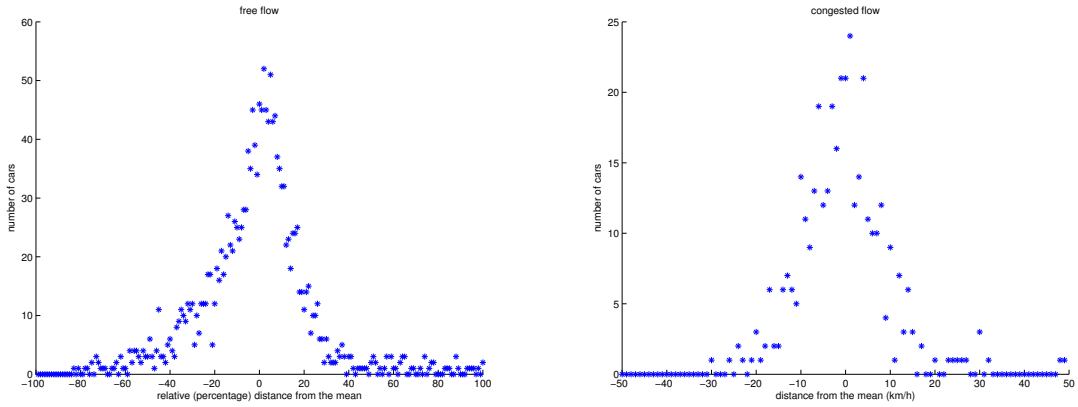

(a) Free flow phase.

(b) Congested phase

Figure 5: Densities of relative distance from the median

particular, we consider measurements taken at km 180, in the direction west-est (Antibes to Nice), and we compare them with the GPS data at the same time and location, see Figure 6. Percentages per hour and per day are collected in Table 1. We can observe that the penetration rate of GPS-equippend vehicles has the same pattern every day: early in the morning the percentage of cars equipped with a COYOTE system is very low (0.9-1.4%), then it starts growing until it reaches the maximum between 9 and 10 a.m. (2.3-3%). Finally it starts decreasing again. This is probably due to the fact that COYOTE systems are mainly used by some specific categories of people such as taxi or truck drivers. Taking a least

Day	6-7 a.m.	7-8 a.m.	8-9 a.m.	9-10 a.m.	10-11 a.m.
1	1.38 %	1.73 %	2.66 %	2.95 %	2.91 %
2	1.36 %	1.74 %	2.31 %	3.00 %	2.28 %
3	0.88 %	1.70 %	2.30 %	2.30 %	2.18 %
4	1.12 %	1.70 %	2.61 %	2.60 %	2.14 %

Table 1: Incoming flux percentage. Km 180, direction 1. Taken from [6].

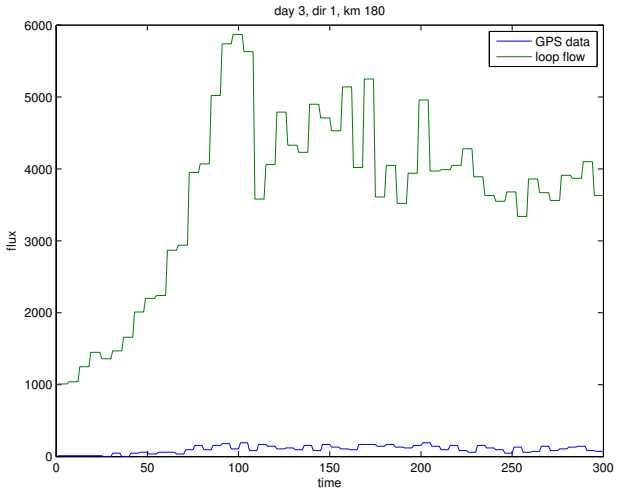

Figure 6: Loop detectors data (6 minutes average, green) and GPS data (blue). March 19, direction 1, km 180.

square interpolation of the percentages of equipped vehicles (Fig. 7a), we obtain rescaled values (Fig. 7b) and we can analyze how the GPS flux varies with respect to the real flux and, consequently, estimate the uncertainty. We firstly compute the rescaled GPS data as

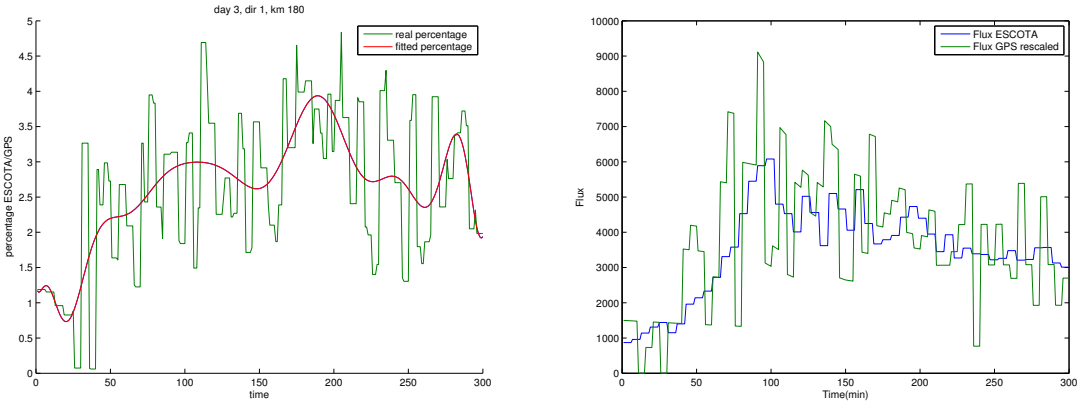

(a) Real and fitted percentages

(b) Loop detectors data and rescaled GPS data.

Figure 7: March 19, direction 1, km 180.

a function of the flux. Since we know when traffic at km 180 is in free or congested flow condition, we can distinguish the flux values (Fig. 8a) and compute the corresponding density through the inverse of the flux function. We eventually compute the relative error as the difference between two fluxes divided by the real one and we can model the perturbation on the initial density as an exponential function of the density multiplied by a random variable X_2:

$$\rho(x;\omega) = \rho(x)\ \left[1 + \beta\ X_2(\omega)\ \exp(-\alpha\ \rho(x))\right], \tag{4.3}$$

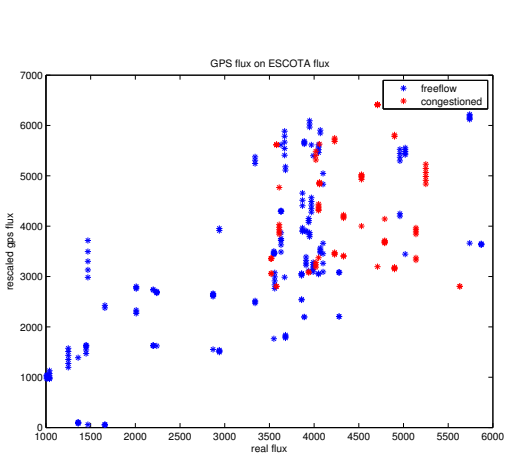

(a) Rescaled GPS density on real density.

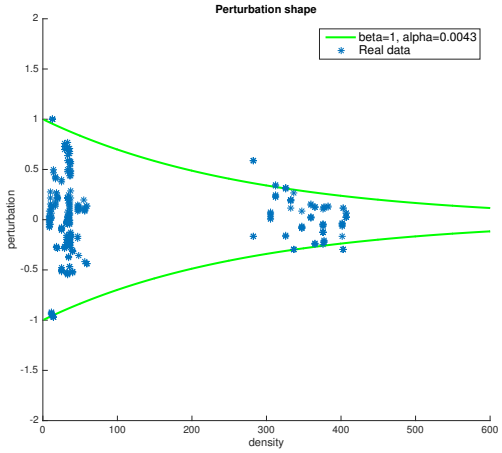

(b) Initial perturbation shaped on real data.

Figure 8: Uncertainty quantification on density values.

where α and β are positive parameters. Fitting the real data, we can set α and β to model the maximal perturbation. Therefore we can find quite easily an exponential function that contains all the data (Fig. 8b). We set the first constraint as a perturbation of 100% in $\rho = 0$, which implies $\beta = 1$, and the second one as a perturbation of 60% in ρ_c. Therefore we use

$$\beta = 1, \quad \alpha = -\frac{\ln(0.6/\beta)}{\rho_c}.$$

We consider a uniform distribution $f_{X_2} = U_{[-1,1]}$. Remark that this choice ensures that the density does not attain negative values.

4.3 A stochastic LWR model for uncertainty quatification in GPS data

We are thus led to consider problem (4.1)

$$F(\rho; X_1(\omega)) := \rho V(\rho; X_1(\omega)) = (1 + X_1(\omega))\rho v(\rho), \qquad f_{X_1} = T_{[-0.5,0,0.5]} \tag{4.4}$$

and

$$\rho_0(x; X_2(\omega)) := \rho(t_0, x) \ [1 + \beta \ X_2(\omega) \ \exp(-\alpha \ \rho(t_0, x))], \qquad f_{X_2} = U_{[-1,1]},$$

where $\rho(t_0, x)$ is the density reconstructed from data at time $t = t_0$, see Section 6.1. In the next sections, we will explain how to estimate the space-time evolution of statistical moments for the above model, and compare the results to our data set.

5 Numerical scheme

We aim at computing approximate solutions $\rho_\Delta(\omega)$ of (4.1) by an iterative procedure $\rho_\Delta^{n+1}(\omega) = \mathcal{H}(\rho_\Delta^n(\omega))$. Following [3], besides the space and time discretization introduced in Section 3, we introduce a partition of the probability space $\Omega \subset \mathbb{R}^s$, i.e. a set of Ω_j, $j = 1, ..., N$, of mutually independent subsets covering Ω:

$$\mu(\Omega_j \cap \Omega_l) = 0 \ \text{ for any } j \neq l, \quad \Omega = \cup_{j=1}^N \Omega_j.$$

We look for approximate solutions of the form

$$\rho_\Delta(t,x,\omega) := \rho_{i,j}^n \quad \text{for } (t,x,\omega) \in [t^n, t^{n+1}[\times[x_{i-1/2}, x_{i+1/2}[\times\Omega_j, \qquad i \in \mathbb{Z}, n \in \mathbb{N}, j = 1, ..., N.$$

For every Ω_j, its probability measure is

$$\mu(\Omega_j) = \int_{\Omega_j} d\mu = \int_{\Omega_j} f_X(X(\omega))\ dX(\omega) \geq 0.$$

Therefore, we want to approximate the solution of (4.1) by the conditional expectation

$$E[\rho_\Delta^{n+1}|\Omega_j] := \frac{1}{\mu(\Omega_j)} \int_{\Omega_j} \rho_\Delta^{n+1}(\omega)\ d\mu = E[\mathcal{H}(\rho_\Delta^n|\Omega_j)]. \tag{5.1}$$

Once the conditional expectation is computed, the mean and the variance of $\rho_\Delta(\omega)$ on the cell C_i at time t^n are given by

$$\bar{\mu}_i^n = \sum_j \mu(\Omega_j)\, E[\rho_\Delta^n|\Omega_j] = \sum_j \rho_{i,j}^n, \quad Var_i^n = \sum_j \int_{\Omega_j} (\rho_\Delta(t^n, x_i, \omega) - \bar{\mu}_i^n)^2\ d\mu = \sum_j \mu(\Omega_j)\ \left(\rho_{i,j}^n - \bar{\mu}_i^n\right)^2.$$

Since the operator $\mathcal{H}$ is nonlinear, we need to compute the conditional expectation $E[g(X)]$ of a function evaluation $g(X)$ in Ω_j, given the conditional expectations $E[X|\Omega_j]$.
For each Ω_j, we wish to find a polynomial $P_j \in \mathbb{P}^p(\mathbb{R}^s)$ of degree p, defined on a stencil S_j, i.e. a set $S_j = \{\Omega_k\}_{k\in I_k}$ with $\Omega_j \in S_j$, such that

$$E[X|\Omega_k] = \frac{1}{\mu(\Omega_k)} \int_{\mathbb{R}^s} 1_{\Omega_k}(\omega)\, P_j(\omega)\ d\mu \qquad \text{for } \Omega_k \in S_j. \tag{5.2}$$

This means that the conditional expectation of the reconstructed polynomial P_j is equal to the conditional expectation of X in each Ω_k of the stencil. Once this polynomial P_j is known, we can estimate

$$E[g(X)] \approx \sum_k \int_{\Omega_k} g(P_j(\omega))\ d\mu$$

by using a quadrature formula in each Ω_k.

We focus now on the case of a one-dimensional probability space $\Omega \subset \mathbb{R}$, the two-dimensional framework being a straightforward generalization.

The Godunov scheme (3.5)–(3.6) applied to (4.1) gives

$$\rho_{i,j}^{n+1} = \rho_{i,j}^n - \frac{\Delta t}{\Delta x}\left(E[h^G(\rho_i^n, \rho_{i+1}^n)|\Omega_j] - E[h^G(\rho_{i-1}^n, \rho_i^n)|\Omega_j]\right). \tag{5.3}$$

As we said before, the expectation of the numerical flux can be approximated as

$$E[h^G(\rho_i^n, \rho_{i+1}^n)|\Omega_j] \approx \frac{1}{\mu(\Omega_j)} \int_{\Omega_j} h^G(P_{i,j}^n(\omega), P_{i+1,j}^n(\omega))\ d\mu, \tag{5.4}$$

where $P_{i,j}$ is a piecewise polynomial reconstruction of the density in the geometric cell C_i and probabilistic cell Ω_j and computed on the stencil S_j.

In order to compute the integral (5.4), we use the third order Gaussian quadrature:

$$\int_a^b h(\omega)d\omega \approx \frac{b-a}{2}\left(h(\xi_1) + h(\xi_2)\right), \tag{5.5}$$

where

$$\xi_1 = \frac{a+b}{2} - \frac{b-a}{2}\frac{\sqrt{3}}{3} \quad \text{and} \quad \xi_2 = \frac{a+b}{2} + \frac{b-a}{2}\frac{\sqrt{3}}{3}. \tag{5.6}$$

Therefore, the integral (5.4) can be computed as:

$$\int_{\Omega_j} h^G(P^n_{i,j}(\omega), P^n_{i+1,j}(\omega))\, f_X(X(\omega))\, dX(\omega)$$
$$\approx \frac{\mu(\Omega_j)}{2}\left(h^G(P^n_{i,j}(\xi_1), P^n_{i+1,j}(\xi_1))f_X(X(\xi_1)) + F(P^n_{i,j}(\xi_2), P^n_{i+1,j}(\xi_2))f_X(X(\xi_2))\right).$$

The most important step is computing the polynomial reconstruction, which defines the order of the method. For any cell Ω_j, we define a polynomial $P_j \in \mathbb{P}^p(\mathbb{R})$ of degree p, described by a stencil $S_j = \{\Omega_j, \Omega_{j_1}, ..., \Omega_{j_p}\}$, where $j_1, ..., j_p \neq j$. Since in the space variable we use a first order finite volume method, we expect that the convergence order will not change increasing the order of the polynomial in the probability space. We will test the approach with a piecewise constant and piecewise linear interpolations (using a MUSCL scheme), analyzing the convergence orders.

- $p = 0$**: first order reconstruction.** We take $S_j = \{\Omega_j\}$ and constant polynomials.
- $p = 1$**: ENO second order reconstruction.** We evaluate two linear polynomials, and take the least oscillatory one. We introduce the average mid-points

  $$\omega_l = E[\xi|\Omega_l].$$

  For the cell Ω_j, we define two polynomials of degree 1: p_j^- is constructed using the cells Ω_{j-1} and Ω_j and p_j^+ is defined on Ω_j and Ω_{j+1}. For p_j^+ we have:

  $$p^+_{i,j}(\omega) = a^+_{i,j}\left(\frac{\omega - \omega_j}{\omega_{j+1} - \omega_j}\right) + b^+_{i,j}, \tag{5.7}$$

  such that

  $$E[p^+_{i,j}|\Omega_j] = E[\rho^n_{i,j}|\Omega_j] \quad \text{and} \quad E[p^+_{i,j}|\Omega_{j+1}] = E[\rho^n_{i,j+1}|\Omega_{j+1}].$$

  Since $E[x - \omega_j|\Omega_j] = 0$ by definition of ω_j, we obtain the 2×2 system

  $$\begin{pmatrix} 1 & 0 \\ 1 & 1 \end{pmatrix}\begin{pmatrix} b^+_{i,j} \\ a^+_{i,j} \end{pmatrix} = \begin{pmatrix} E(\rho^n_{i,j}|\Omega_j) \\ E(\rho^n_{i,j+1}|\Omega_{j+1}) \end{pmatrix}. \tag{5.8}$$

  and similarly forl $p^-_{i,j}(\omega) = a^-_{i,j}\dfrac{\omega - \omega_j}{\omega_{j+1} - \omega_j} + b^-_{i,j}$. From (5.7) and (5.8), we recover

  $$p^+_{i,j}(\omega) = \left(E(\rho^n_{i,j+1}|\Omega_{j+1}) - E(\rho^n_{i,j}|\Omega_j)\right)\left(\frac{\omega - \omega_j}{\omega_{j+1} - \omega_j}\right) + E(\rho^n_{i,j}|\Omega_j),$$

  $$p^-_{i,j}(\omega) = \left(E(\rho^n_{i,j}|\Omega_j) - E(\rho^n_{i,j-1}|\Omega_{j-1})\right)\left(\frac{\omega - \omega_{j-1}}{\omega_j - \omega_{j-1}}\right) + E(\rho^n_{i,j-1}|\Omega_{j-1}).$$

  We choose $P^n_{i,j}$ equal to the one that realizes the least oscillation: $\min\left\{\left|E(\rho^n_{i,j+1}|\Omega_{j+1}) - E(\rho^n_{i,j}|\Omega_j)\right|, \left|E(\right.\right.$

  The procedure is summarized in Algorithm 1.

5.1 Numerical tests

To validate the approach, we show some results concerning the stochastic conservation law (4.1) with random flux function (4.4) without capacity drop and piece-wise constant (deterministic) initial datum $\rho_0(x) = \rho_L = 10$ for $x < x_0$ and $\rho_0(x) = \rho_R = 80$ for $x > x_0$, $x_0 = 0.5$. In this case the mean and the variance can be computed analytically: for each realization of the random variable, the solution is given by a shock wave moving with speed

$$\sigma(\rho_L, \rho_R; \omega) = (1 + X_1(\omega)) \frac{\rho_L v(\rho_L) - \rho_R v(\rho_R)}{\rho_L - \rho_R} ,$$

and we deduce

$$\bar{\mu}(t,x) = \int_{-\infty}^{\frac{x-x_0}{\sigma(\rho_L,\rho_R;\omega)t}-1} \rho_L f_{X_1}(y)\, dy + \int_{\frac{x-x_0}{\sigma(\rho_L,\rho_R;\omega)t}-1}^{+\infty} \rho_R f_{X_1}(y)\, dy,$$

$$Var(t,x) = \int_{-\infty}^{\frac{x-x_0}{\sigma(\rho_L,\rho_R;\omega)t}-1} (\rho_L - \bar{\mu}(t,x))^2 f_{X_1}(y)\, dy + \int_{\frac{x-x_0}{\sigma(\rho_L,\rho_R;\omega)t}-1}^{+\infty} (\rho_R - \bar{\mu}(t,x))^2 f_{X_1}(y)\, dy.$$

We consider both uniform and triangular probability distributions and the piece-wise constant and ENO polynomial reconstructions described above, which give similar results. Figures 9 and 10 show the results obtained with the ENO reconstruction for $\Delta x = 0.01$ and $\Delta x = 0.002$ respectively, and $N = 40$ probabilistic cells in $[-1, 1]$.

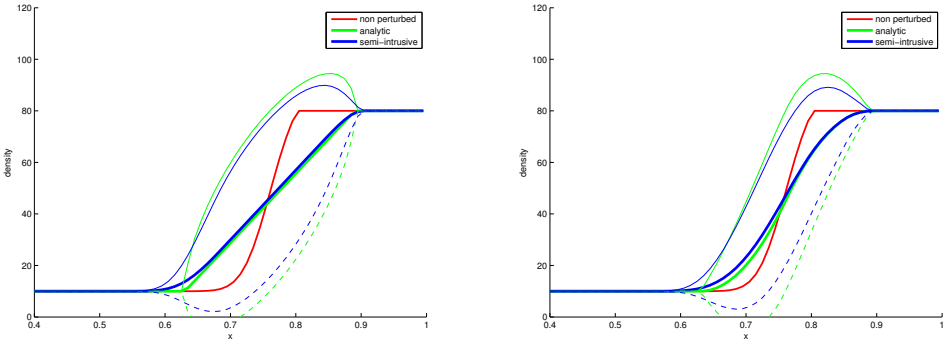

(a) Uniform distribution **(b)** Triangular distribution

Figure 9: Deterministic solution (red), analytic (green) and computed (blue) mean and standard deviation for $\Delta x = 0.01$.

To analyze the L_1-convergence for the two polynomial reconstructions, we denote by $\bar{\mu}_\Delta$ and $\bar{\mu}$ respectively the means computed by the semi-intrusive method and analytically. We then keep fixed the space mesh, while refining the probabilistic discretization, and compute the error

$$err(\Delta) = \|\bar{\mu}_\Delta - \bar{\mu}\|_{L^1}.$$

Figure 11a shows that the errors corresponding to the first and second order interpolations are very close, since they are conditioned by the first order spatial approximation. Figure 11b displays the probabilistic convergence curves for $N = 2, \ldots, 2^{10}$, corresponding to different space

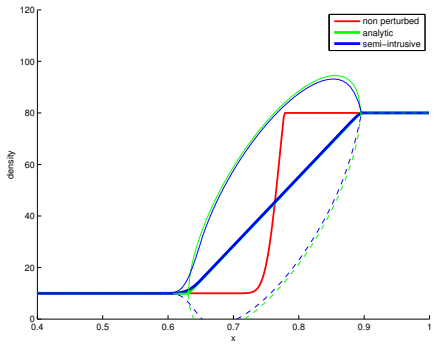

(a) Uniform distribution

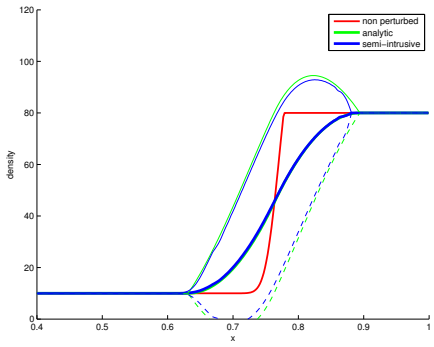

(b) Triangular distribution

Figure 10: Deterministic solution (red), analytic (green) and computed (blue) mean and standard deviation for $\Delta x = 0.002$.

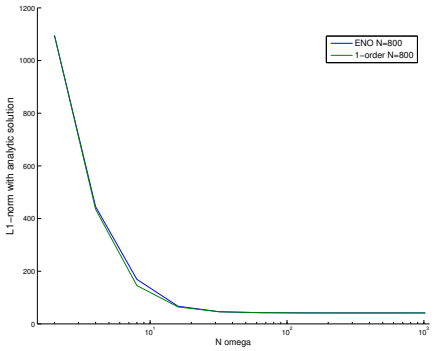

(a) First order and ENO reconstructions

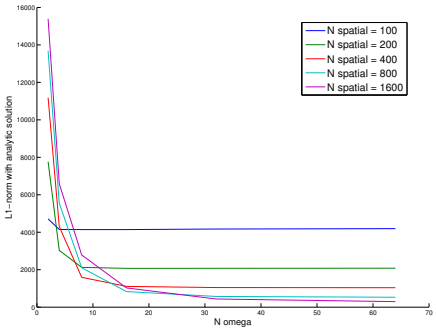

(b) Error curves for different spatial mesh sizes

Figure 11: Convergence analysis in the probabilistic direction.

mesh sizes $\Delta x = 2^{-n}10^{-2}$, $n = 1, \ldots, 4$. This confirms that if the probabilistic discretization is fine enough, the main contribution comes from the spatial error.

To evaluate the computing time, we compare the Abgrall-Congedo approach using a piecewise constant polynomial reconstruction of the density with the Monte Carlo method. Figure 12 plots the time as a function of the L^1-error, for $\Delta x = 0.001$ and a triangular distribution $T_{[-0.5,0,0.5]}$ for the speed perturbation. We remark that the Abgrall-Congedo approach is significantly faster than Monte Carlo. See also Table 2.

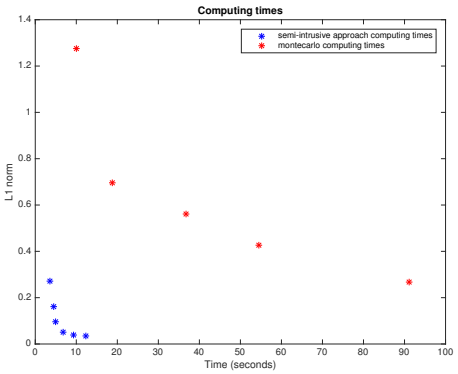

Figure 12: Computing time for a Riemann problem with $N_x = 1000$.

A-C		MC	
Time	Error	Time	error
3.2	0.40	19.3	0.40
3.5	0.28	37.6	0.31
3.7	0.20	55.9	0.37
3.9	0.15	112.0	0.16

Table 2: Computing times for Abgrall-Congedo approach and Monte Carlo.

6 Uncertainty quantification in traffic flow simulations

6.1 Model calibration

We calibrate the fundamental diagram following [6, Section 5]. In particular, for the section around km 180 in direction 1, we take $v_{max} = 125$ km/h, $\omega_f = 17$ km/h, $\rho_{max} = 614$ vehicles/km, $\rho_c = 120$ vehicles/km and $\rho_a = 300$ vehicles/km.

To estimate the initial conditions at some fixed time $t_0 \geq 6:00$ am, for every space cell C_i, we consider a weighted average of the data measured in the hour preceding time t_0, with an exponentially decreasing weight (for more details see [6, 8]):

$$\alpha_i(t_k, t_0) = \begin{cases} 0 & \text{if } t_0 - t_k < 0, \\ e^{\dfrac{(t_k - t_0)}{a}} & \text{if } 0 \leq t_0 - t_k < 60, \\ 0 & \text{if } t_0 - t_k \geq 60. \end{cases} \tag{6.1}$$

Then, as initial condition, we compute $\rho_i^{t_0}$ as

$$\rho_i^{t_0} := \frac{1}{\sum_{k=0}^{n} \alpha_i(t_k, t_0)} \sum_{k=0}^{n} \alpha_i(t_k, t_0)\ \rho_i^{data}(t_k)\,, \tag{6.2}$$

where $\rho_i^{data}(t_k)$ is the density measured in cell C_i at time t_k. The coefficient a depends on the reliability of the data and on the variability of the traffic in the hour before t_0. After some tests, we decided to fix $a \in [1.5, 2]$ to give more importance at data close to t_0 and we increase it if we need to consider a longer period.

To avoid dealing with boundary conditions, we run simulations on a larger space domain so that information coming from upstream and downstream boundaries do not reach the domain of interest.

6.2 Uncertainty on the mean velocity

For the speed uncertainty, we use the Abgrall-Congedo approach using piece-wise constant polynomials. The triangular distribution $T_{[-0.5,0,0.5]}$ is discretized in 20 cells and we set $t_0 =$ 9:00 am. We remark that when a constant interpolation is used, the approach is not very different from Monte Carlo methods, but the computational time is drastically reduced, see Section 5.1. We plot the speed evolution for $X_1 = 0$ in Fig. 13a and the mean and standard deviations in Fig. 13b. In both cases, we compare the simulation results with the real values. We observe that the results of the simulation fit the behavior of the actual data and most of the values fall in the standard deviation range.

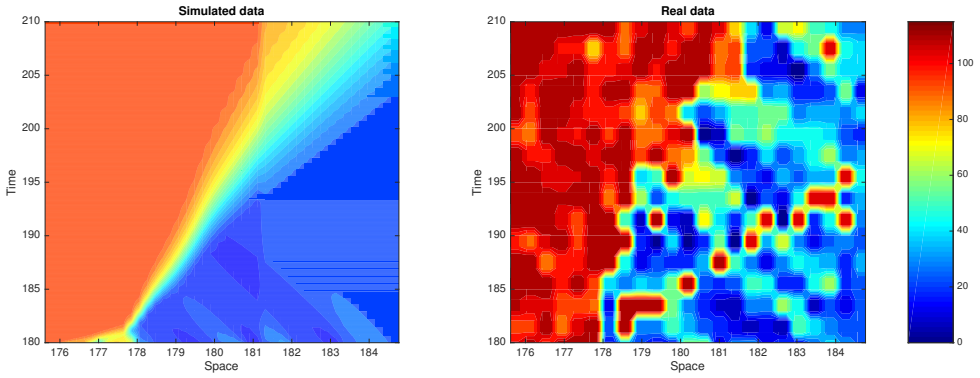

(a) Antibes to Saint-Laurent-du-Var April 2, 2013, 9 - 9:30am: speed simulation results (left) VS real data (right).

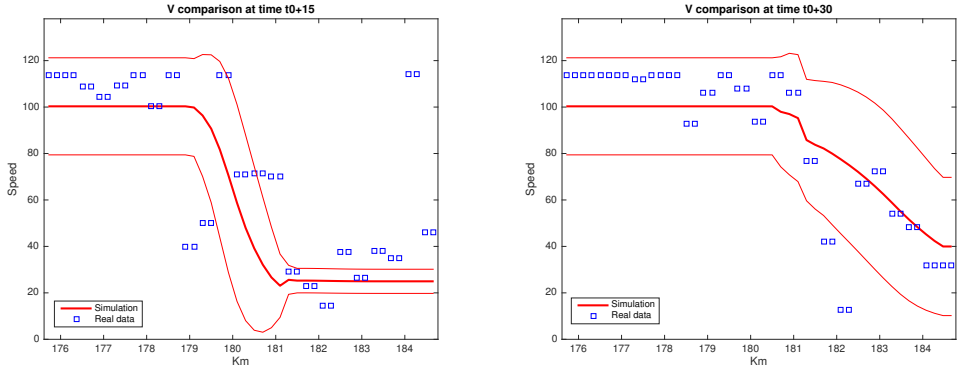

(b) Computed mean speed ± standard deviation (red) and real data (blue) at $t_0 + 15$ and $t_0 + 30$.

Figure 13: Speed uncertainty.

6.3 Uncertainty on the initial condition

We analyze here the influence of a perturbation on the initial density. The goal is to find the variance corresponding to the actual variability due to the lack of data. Unfortunately, we saw in Section 4.2 that our data cover only a very low percentage of the actual values. Consequently, when we fit the variability, we found a non-linear perturbation which has high values. This implies a loss of significance in our model. Actually, when we apply the

perturbation to a real case (we use the above-mentioned example), we can notice that the standard deviation dramatically increases (Fig. 14).

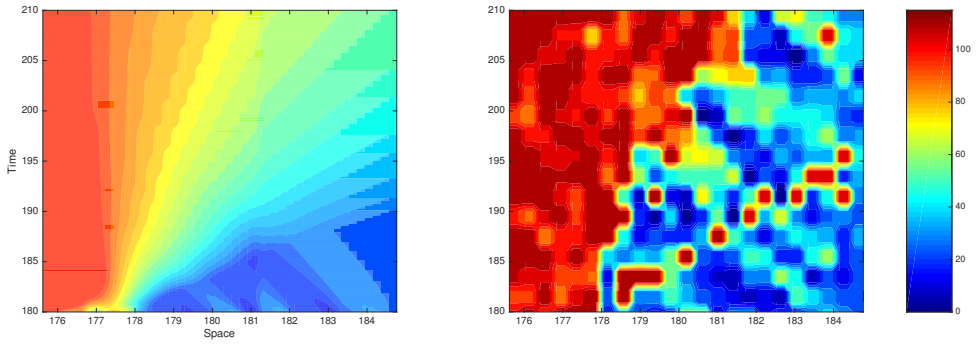

(a) Antibes to Saint-Laurent-du-Var April 2, 2013, 9 - 9:30am: speed simulation results (left) VS real data (right).

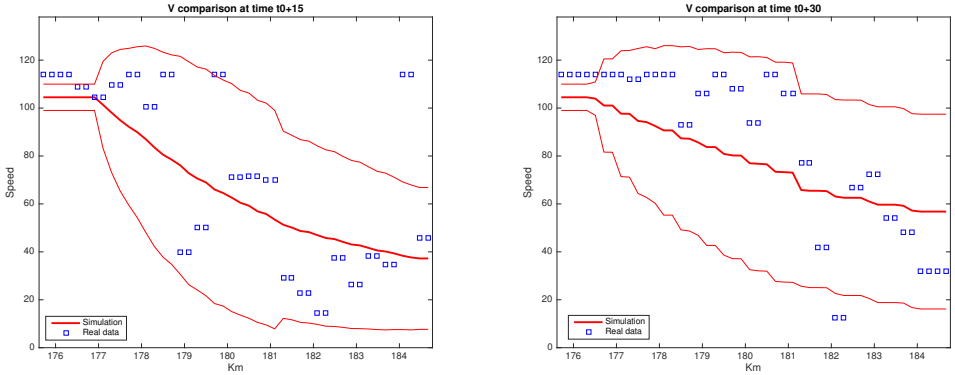

(b) Computed mean speed ± standard deviation (red) and real data (blue) at $t_0 + 15$ and $t_0 + 30$.

Figure 14: Initial density uncertainty.

6.4 Complete uncertainty estimation

Considering both speed and initial data uncertainties in the model, we have to deal with a two dimensional probability space. Following Section 4.3, we note $\omega_1 \in \Omega^1 = \cup_j \Omega^1_j$ the speed random parameter and $\omega_2 \in \Omega^2 = \cup_l \Omega^2_l$ the initial density one, and assume they are independent. Using Algorithm 1, we define

$$\bar{\mu}^n_i = \sum_{j,l} \rho^n_{i,j,l}\, \mu_1(\Omega^1_j)\mu_2\Omega^2_l)$$

and

$$\bar{\mu}^n_{i,j} = \sum_l \rho^n_{i,j,l}\, \mu_2(\Omega^2_l), \qquad \bar{\mu}^n_{i,l} = \sum_j \rho^n_{i,j,l}\, \mu_1(\Omega^1_j),$$

respectively

$$Var^n_{i,j} = \sum_l \left(\rho^n_{i,j,l} - \bar{\mu}^n_{i,j}\right)^2 \mu_2(\Omega^2_l), \qquad Var^n_{i,l} = \sum_j \left(\rho^n_{i,j,l} - \bar{\mu}^n_{i,l}\right)^2 \mu_1(\Omega^1_j).$$

Remark that, by the law of total variance, we can compute

$$\begin{aligned} Var_i^n &= \sum_{j,l} (\rho_{i,j,l}^n)^2 \, \mu_1(\Omega_j^1)\mu_2(\Omega_l^2) - (\bar{\mu}_i^n)^2 \\ &= \sum_l \mu_2(\Omega_l^2) \sum_j \left(\rho_{i,j,l}^n - \bar{\mu}_{i,l}^n\right)^2 \mu_1(\Omega_j^1) + \sum_l \left(\bar{\mu}_{i,l}^n - \mu_i^n\right)^2 \bar{\mu}_2(\Omega_l^2) \\ &= Mean(Var_{i,l}^n) + Var(\bar{\mu}_{i,l}^n). \end{aligned}$$

We report in Figure 15 the approximated mean and standard deviation corresponding to the section between Antibes and Saint-Laurent-du-Var on April 2, 2013, 9 - 9:30 am. We observe that the standard deviation is very close to the previous case in Section 6.3, where only the initial density perturbation was considered. This can be explained by the fact that, in our specific case, the information on density is poor and the variability of the initial datum is very large.

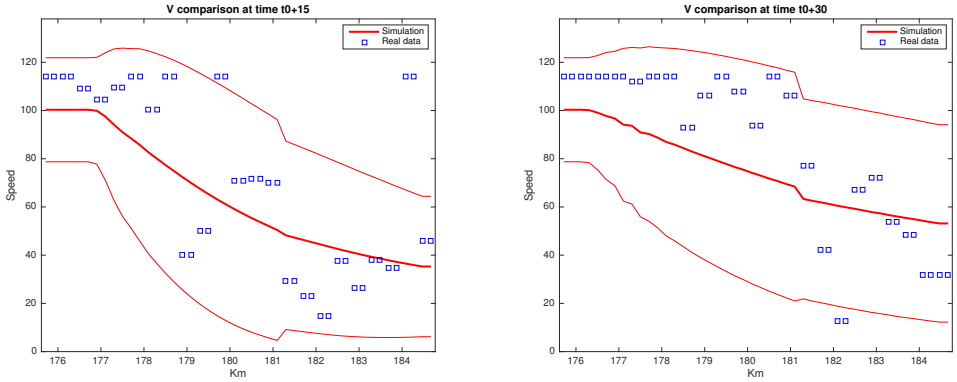

Figure 15: Speed and initial density uncertainties. Computed mean speed ± standard deviation (red) and real data (blue) at $t_0 + 15$ and $t_0 + 30$.

6.5 Travel time estimation

Uncertainty quantification can be extended to travel time predictions. Since each car in the data set has an identification label, we know the time needed to cover a certain distance. Besides, numerical simulations allow us to compute travel times from mean velocities, and their mean and standard deviation. We report in the following figures the travel times in a space-time plot: in red the trajectory of a selected vehicle in the data set, in blue the computed mean and in green the computed mean ± its standard deviation. We observe that the forecasts are good when the traffic is in free flow or congested, see Figures 16 and 17. On the contrary, when traffic conditions change, like in Figure 18, initial conditions are not sufficient to have good results and information about boundary inflow and outflow become essential.

7 Conclusion

In this paper, we have proposed a stochastic macroscopic traffic flow model accounting for GPS data uncertainty. We used an efficient semi-intrusive numerical method to evaluate

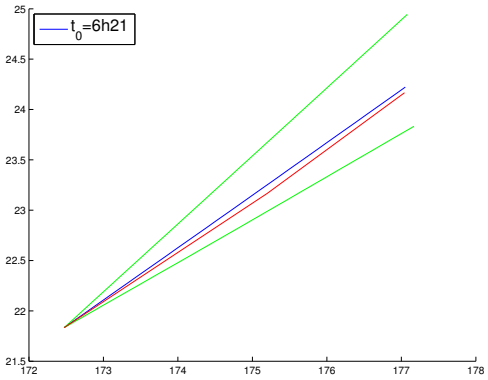

(a) $t_0 = 06:20$

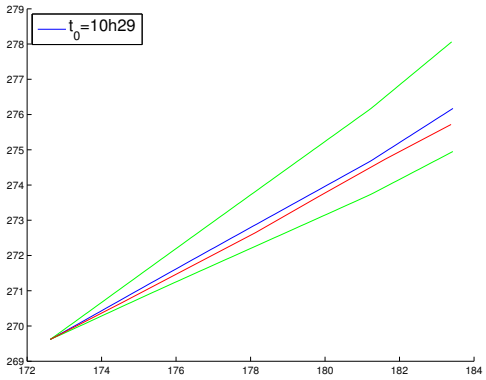

(b) $t_0 = 10:29$

Figure 16: Space-time plots of computed mean travel (blue) ± st.deviation (green) and actual travel (red) when the traffic is in free-flow.

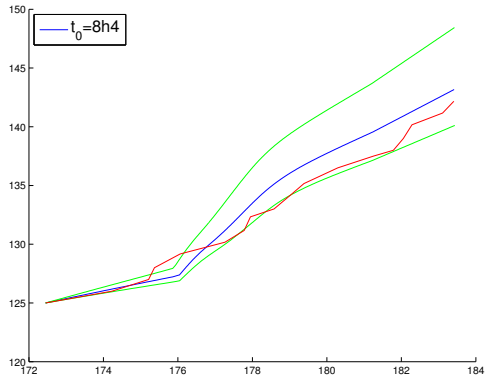

(a) $t_0 = 08{:}04$ am

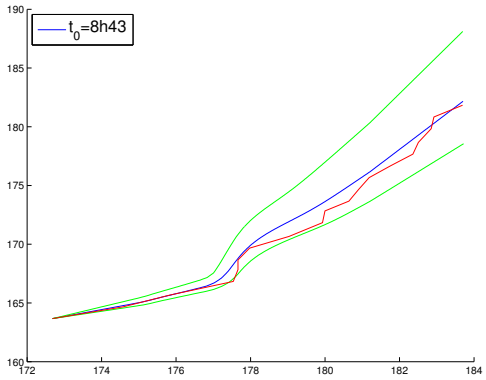

(b) $t_0 = 08{:}43$ am

Figure 17: Space-time plots of computed travel (blue) ± st.deviation (green) and actual travel (red) when the traffic is congested.

uncertainty propagation in traffic simulations and we tested the results against real data collected on a busy sector of the French A8 highway close to Nice. The results are quite satisfactory, in particular when traffic does not change phase. From the application point of view, these preliminary results can be improved considering higher order finite volume methods for the spatial discretization, and taking into account boundary conditions and their uncertainty. Besides, well-posedness of stochastic conservation laws with discontinuous flux function needs to be investigated.

Acknowledgments

This research was mainly carried out during the first author's internship at Inria Sophia Antipolis Méditerranée.

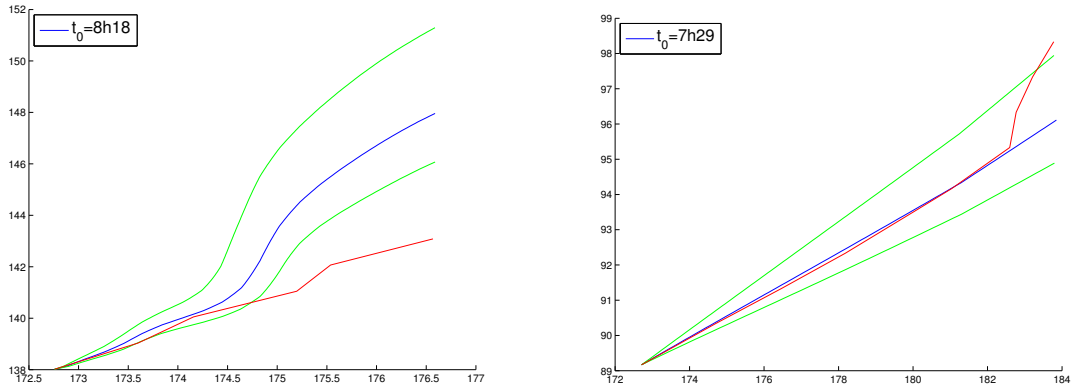

(a) $t_0 = 08{:}18$ am **(b)** $t_0 = 07{:}29$ am

Figure 18: Space-time plots of computed travel (blue) ± st.deviation (green) and actual travel (red) when the traffic phase changes (from congested to free flow **(a)** and from free flow to congested **(b)**).

References

[1] Autoroutes Trafic. `http://www.autoroutes-trafic.fr/`. Accessed: 2019-07-28.

[2] Escota (VINCI Autoroutes). `https://corporate.vinci-autoroutes.com/fr/presentation/societes-vinci-autoroutes/escota/en-bref`. Accessed: 2019-07-28.

[3] R. Abgrall and P. M. Congedo. A semi-intrusive deterministic approach to uncertainty quantification in non-linear fluid flow problems. *Journal of Computational Physics*, 235:828–845, 2013.

[4] R. Boel and L. Mihaylova. A compositional stochastic model for real time freeway traffic simulation. *Transportation Research Part B: Methodological*, 40(4):319–334, 2006.

[5] M. Bulíček, P. Gwiazda, J. Málek, and A. Świerczewska Gwiazda. On scalar hyperbolic conservation laws with a discontinuous flux. *Math. Models Methods Appl. Sci.*, 21(1):89–113, 2011.

[6] A. Cabassi and P. Goatin. Validation of traffic flow models on processed GPS data. Research Report RR-8382, INRIA, 2013.

[7] K.-C. Chu, L. Yang, R. Saigal, and K. Saitou. Validation of stochastic traffic flow model with microscopic traffic simulation. In *2011 IEEE International Conference on Automation Science and Engineering*, pages 672–677. IEEE, 2011.

[8] E. Cristiani, C. de Fabritiis, and B. Piccoli. A fluid dynamic approach for traffic forecast from mobile sensor data. *Communications in Applied and Industrial Mathematics*, 1(1):54–71, 2010.

[9] C. F. Daganzo. The cell transmission model: A dynamic representation of highway traffic consistent with the hydrodynamic theory. *Transportation Research Part B: Methodological*, 28(4):269–287, 1994.

[10] J. a.-P. Dias, M. Figueira, and J.-F. Rodrigues. Solutions to a scalar discontinuous conservation law in a limit case of phase transitions. *J. Math. Fluid Mech.*, 7(2):153–163, 2005.

[11] M. Garavello and B. Piccoli. *Traffic flow on networks*, volume 1 of *AIMS Series on Applied Mathematics*. American Institute of Mathematical Sciences (AIMS), Springfield, MO, 2006. Conservation laws models.

[12] T. Gimse. Conservation laws with discontinuous flux functions. *SIAM J. Math. Anal.*, 24(2):279–289, 1993.

[13] S. K. Godunov. A difference method for numerical calculation of discontinuous solutions of the equations of hydrodynamics. *Mat. Sb. (N.S.)*, 47 (89):271–306, 1959.

[14] S. E. Jabari and H. X. Liu. A stochastic model of traffic flow: Theoretical foundations. *Transportation Research Part B: Methodological*, 46(1):156–174, 2012.

[15] J.-P. Lebacque. The Godunov scheme and what it means for first order traffic flow models. In *Transportation and traffic theory. Proceedings of the 13th international symposium on transportation and traffic theory, Lyon, France, 24-26 JULY 1996*, 1996.

[16] J. Li, Q.-Y. Chen, H. Wang, and D. Ni. Analysis of LWR model with fundamental diagram subject to uncertainties. *Transportmetrica*, 8(6):387–405, 2012.

[17] M. J. Lighthill and G. B. Whitham. On kinematic waves II. A theory of traffic flow on long crowded roads. *Proceedings of the Royal Society of London. Series A. Mathematical and Physical Sciences*, 229(1178):317–345, 1955.

[18] S. Mishra, N. H. Risebro, C. Schwab, and S. Tokareva. Numerical solution of scalar conservation laws with random flux functions. *SIAM/ASA J. Uncertain. Quantif.*, 4(1):552–591, 2016.

[19] S. Mishra and C. Schwab. Sparse tensor multi-level Monte Carlo finite volume methods for hyperbolic conservation laws with random initial data. *Math. Comp.*, 81(280):1979–2018, 2012.

[20] G. F. Newell. A simplified theory of kinematic waves in highway traffic, part II: Queueing at freeway bottlenecks. *Transportation Research Part B: Methodological*, 27(4):289–303, 1993.

[21] G. Poëtte, B. Després, and D. Lucor. Uncertainty quantification for systems of conservation laws. *J. Comput. Phys.*, 228(7):2443–2467, 2009.

[22] P. I. Richards. Shock waves on the highway. *Operations research*, 4(1):42–51, 1956.

[23] V. Schleper. A hybrid model for traffic flow and crowd dynamics with random individual properties. *Math. Biosci. Eng.*, 12(2):393–413, 2015.

[24] A. Sumalee, R. Zhong, T. Pan, and W. Szeto. Stochastic cell transmission model (SCTM): A stochastic dynamic traffic model for traffic state surveillance and assignment. *Transportation Research Part B: Methodological*, 45(3):507–533, 2011.

[25] M. Treiber and A. Kesting. *Traffic flow dynamics*. Springer, Heidelberg, 2013. Data, models and simulation, Translated by Treiber and Christian Thiemann.

[26] J. Tryoen, O. Le Maître, and A. Ern. Adaptive anisotropic spectral stochastic methods for uncertain scalar conservation laws. *SIAM J. Sci. Comput.*, 34(5):A2459–A2481, 2012.

[27] H. Wang, D. Ni, Q.-Y. Chen, and J. Li. Stochastic modeling of the equilibrium speed–density relationship. *Journal of Advanced Transportation*, 47(1):126–150, 2013.

[28] J. K. Wiens, J. M. Stockie, and J. F. Williams. Riemann solver for a kinematic wave traffic model with discontinuous flux. *J. Comput. Phys.*, 242:1–23, 2013.

[29] D. B. Work, S. Blandin, O.-P. Tossavainen, B. Piccoli, and A. M. Bayen. A traffic model for velocity data assimilation. *Appl. Math. Res. Express. AMRX*, (1):1–35, 2010.

Supplementary

Semi-intrusive deterministic algorithm

while $t < T$: ***Deterministic loop*** *on time:* **do**
  $t = t + \Delta t$
  for *i:=1 to size(ρ) : Deterministic loop on space:* **do**
    for *j:=1 to size(Ω) :* ***Probabilistic loop:*** **do**
      Calculate $a^+_{i,j}, a^-_{i,j}, b^+_{i,j}, b^-_{i,j}$;
      Calculate polynomial $p_{i,j}$ evaluated in ξ_1 and ξ_2 that satisfies
      $\min\left\{\left|a^+_{i,j}\right|, \left|a^-_{i,j}\right|\right\}$;
      for $\omega := \xi_1, \xi_2$*:* ***Quadrature loop:*** **do**
        Compute Godunov flux approximations as function of ω:

$$h^G(P^n_{i,j}(\omega), P^n_{i+1,j}(\omega)) \quad \text{and} \quad h^G(P^n_{i-1,j}(\omega), P^n_{i,j}(\omega));$$

      end
      Compute expectancies $E\left[h^G(\rho^n_{i,j}, \rho^n_{i+1,j})|\Omega_j\right]$ using quadrature formula;
      Update values

$$\rho^{n+1}_{i,j} = \rho^n_{i,j} - \frac{\Delta t}{\Delta x}\left(E\left[h^G(\rho^n_{i,j}, \rho^n_{i+1,j})|\Omega_j\right] - E\left[h^G(\rho^n_{i-1,j}, \rho^n_{i,j})|\Omega_j\right]\right);$$

    end
  end
end

Algorithm 1: Semi-intrusive method